Modifying an Affordable ROV for Under-ice Sensing

Lin Zhao
Department of Ocean Engineering
University of Rhode Island
Narragansett, RI, USA
linzhao@uri.edu

Mingxi Zhou
Graduate School of Oceanography
University of Rhode Island
Narragansett, RI, USA
mzhou@uri.edu

Brice Loose
Graduate School of Oceanography
University of Rhode Island
Narragansett, RI, USA
bloose@uri.edu

Virginia Cousens
Graduate School of Oceanography
University of Rhode Island
Narragansett, RI, USA
gcousens@uri.edu

Raymond Turrisi
Department of Mechanical, Industrial and Systems Engineering
University of Rhode Island
Kingston, RI, USA
raymond_turrisi@uri.edu

***Abstract*—An affordable Remotely Operated Vehicle (ROV) has been modified for under-ice sensing. In this paper, we present the system upgrade, including sensor integration, electronics and navigation stack. The new ROV is equipped with a Doppler Velocity Log (DVL) and an attitude heading reference system (AHRS) for navigation, and a stereo camera and a forward-looking imaging sonar for perception. Field experiments were conducted in March 2021 on a frozen waterway in Michigan. The ROV was controlled to stay within 2 meters away from the ice keel. Dead-reckoning navigation based on the DVL, AHRS and Extended Kalman Filter (EKF) are implemented with results presented in the paper. Using the navigation result and DVL beam range measurements, ice-thickness was estimated along the vehicle's path. The ice thickness is found to be about 25 to 30 cm that is coincident with manual observation from drilled ice holes. Besides that, we also present and discuss interesting features embedded in the frozen ice observed by our stereo camera and the forward-looking imaging sonar.**

***Index Terms*—Remotely Operated Vehicle (ROV), Under-ice Navigation, Extended Kalman Filter (EKF)**

I. Introduction

The ocean in polar regions plays a vital role in affecting global overturning circulation, biological pumping, and carbon cycle ([1]–[4]). Sparse in-situ measurements from ice coring [5] and tethered sampling stations [6] have revealed fascinating physical and biogeochemical processes in this region, such as biological plume, air bubbles [7], sub-platelet layers [8], and basal ice melting [9]. In fact, our understanding of these physical and biogeochemical processes, especially their spatial extent, is still limited because they are severely under-sampled due to the existence of ice. Ice coring and ice-tethered platforms are still popular for sampling the ocean under the ice. However, these approaches prefer thinner ice [10] that is more accessible, and they deform the ice structure during anchoring and coring [11]. As a result, the measurements may be subject to bias. They are also sparsely placed, sufficient for observing large-scale (over 10 km) processes, but, fail to detect and quantify smaller sub-mesoscale phenomena.

Robotic platforms, i.e., Autonomous Underwater Vehicles (AUVs), are a highly promising tool for obtaining high-resolution spatial coverages on small-scale biogeochemical processes under the ice. Almost all the AUVs are initially developed for open-water applications. Thus, a long list of modifications needs to be made for under-ice sampling [12].

In this paper, we present our progress on modifying an affordable ROV for under-ice sensing. The remaining paper is organized as follows. In Section II, we will review related works on AUV-based under-ice operations. The ROV sensor integration and navigation system are discussed in Section III and Section IV. Under-ice field tests have been conducted with results shown in Section V. We will conclude the paper and introduce our future works in Section VI.

II. Related works

Operating AUVs under the ice is challenging, but it does not prevent researchers from pushing the frontier of AUV-based under-ice explorations. During the Spinnaker project [13] in the 1980s, the Theseus AUV, an 8-meter-long vehicle, was deployed under the ice in the Arctic. The AUV traveled hundreds of kilometers to lay communication cables on the seabed for detecting foreign submarines that may travel under permanent ice through deep channels. Several notable under-ice AUV deployments were performed in the 21st Century. Following the first under-ice sidescan image collection from an AUV in 2002 [14], several groups from the USA, UK, and Japan accomplished multiple transects under ice floes and obtained underside ice topography. Autosub another large-size AUV has been developed and deployed for under-ice sensing [15] [16]. The AE2000a AUV was deployed in the Okhotsk Sea to map the underside of an ice floe using a multibeam

This work is supported by the National Science Foundation (NSF) under the award #1945924, and the Graduate School of Oceanography, University of Rhode Island. We also thank the field support from the Great Lake Research Center, Michigan Technological University.

sonar [17]. Another seminal under-ice mapping operation was done in 2015 [18] with the SEABED [19], a twin-hull AUV, where the AUV performed lawnmower-pattern surveys under several ice floes. The result, 3D topography maps, enabled an accurate characterization of the physical dimensions of the surveyed ice floes. More recently, a Kongsberg HUGIN AUV was deployed to fly under the Thwaite Glacier ice shelf for seabed mapping and water column assessment [20]. While the above AUVs are relatively large, several research groups have looked into compact and affordable AUVs, such as the Gavia AUV [21]–[23], REMUS AUV [24], Seagliders [25], and Icefin [26], which are easier to operate (without ice camp or icebreakers) at relatively lower prices, but with limited sensing capability and endurance. Among these successful under-ice AUVs, there are few deployments targeted at exploring the ice-water boundary layer that is within 4 meters under the bottom of the ice. Rather, most of the AUVs were programmed to fly at a constant depth further away from the ice and used upward-looking sonar to map the ice bottom topography, which only provides limited information on the existence of sub-ice platelet layers, macroalgae plumes, or radiance budget.

III. Under-ice ROV design

We selected BlueROV-2 platform as our test bed since they are open-source and has a wide user community. Due to the lack of sensors on the base BlueROV model for a good localization result, we integrated a suit of sensors to greatly improve the visual sensing and navigation capability of the vehicle.

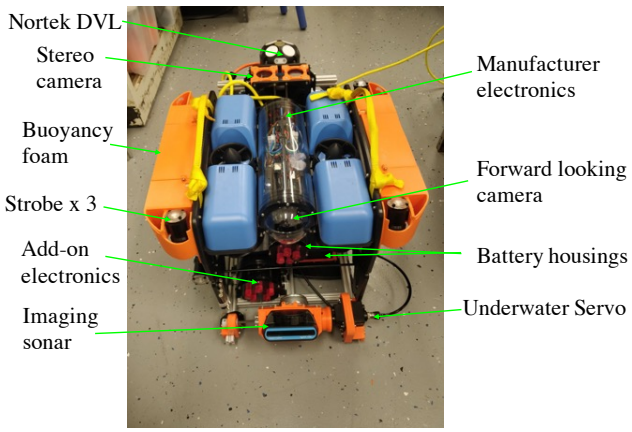

Fig. 1. The Modified BlueROV for under-ice sensing

Figure 1 shows the upgraded BlueROV for under-ice sensing. For navigation and collision avoidance, we have integrated an upward-looking Doppler Velocity Log (DVL) from Nortek Inc., an attitude heading reference system (Parker Lord MicroStrain), and a forward-looking image sonar (Blueprint Subsea). For ice sensing, we have developed a stereo camera system mounted in an upward-looking configuration. Two Li-ion battery packs are integrated in separated pressure housings, providing an overall energy of about 500 Watt-hour. All the electronics are enclosed inside a 4-inch aluminum pressure housing in the lower level. A Jetson NX Xavier embeded computer is integrated to interface with all the add-on sensors using the Robotic Operating System (ROS) middleware. On the topside computer, we have the BlueROV user-interface for remote control and a customized RViz interface for visualizing perceptual sensor measurements.

IV. Navigation System

In order to deploy the localization method into the ROV for real-time processing in the future, Extended Kalman Filter (EKF) [27] framework is selected for its low computational cost. A ROS package, robot localization [28], is used to fuse multiple sensors with different sources (e.g. IMU, velocity, odometry) using EKF. EKF implemented in robot localization will be reviwed in this section first. Then, we will present our EKF setup and parameters tested with our field data.

A. Extended Kalman Filter

The estimation process can be described as a nonlinear dynamic system

$$\boldsymbol{x}_k = f(\boldsymbol{x}_{k-1}) + \boldsymbol{w}_{k-1} \tag{1}$$

where $\boldsymbol{x}_k = [x, y, z, \phi, \theta, \psi, u, v, w, p, q, r, \dot{u}, \dot{v}, \dot{w}]^T$ presenting vehicle's 15 states at time k, including position (x, y, z), orientation expressed by Euler angle roll, pitch and yaw (ϕ, θ, ψ), body-frame linear velocities (u, v, w), angular velocities (p, q, r) and linear accelerations $(\dot{u}, \dot{v}, \dot{w})$. f is the nonlinear state transition function, $\boldsymbol{w}_{k-1}$ is the process noise, which is assumed to be a Gaussian distribution.

The measurement model is

$$\boldsymbol{z}_k = h(\boldsymbol{x}_k) + \boldsymbol{v}_k \tag{2}$$

where $\boldsymbol{z}_k$ is the measurement at time k, h is the nonlinear sensor model which relates the state $\boldsymbol{x}_k$ to the measurement $\boldsymbol{z}_k$, $\boldsymbol{v}_k$ is the measurement noise, which is a Gaussian distribution.

Prediction equations, also known as state and covariance propagation, are shown in the following equations.

$$\hat{\boldsymbol{x}}_k = f(\boldsymbol{x}_{k-1}) \tag{3}$$

$$\hat{\boldsymbol{P}}_k = \boldsymbol{F}\boldsymbol{P}_{k-1}\boldsymbol{F}^T + \boldsymbol{Q} \tag{4}$$

where f is a standard 3D kinematic model derived from Newtonian mechanics. The state propagation function can be a nonlinear function. The covariance, $\boldsymbol{P_k}$, is updated based on $\boldsymbol{F}$, the Jacobian of f, and $\boldsymbol{Q}$, the process noise covariance.

The measurement update equations are shown in Eq.5 to 7

$$\boldsymbol{K} = \hat{\boldsymbol{P}}_k\boldsymbol{H}^T(\boldsymbol{H}\hat{\boldsymbol{P}}_k\boldsymbol{H}^T + \boldsymbol{R})^{-1} \tag{5}$$

$$\boldsymbol{x}_k = \hat{\boldsymbol{x}}_k + \boldsymbol{K}(\boldsymbol{z} - \boldsymbol{H}\hat{\boldsymbol{x}}_k) \tag{6}$$

$$\boldsymbol{P}_k = (\boldsymbol{I} - \boldsymbol{K}\boldsymbol{H})\hat{\boldsymbol{P}}_k(\boldsymbol{I} - \boldsymbol{K}\boldsymbol{H})^T + \boldsymbol{K}\boldsymbol{R}\boldsymbol{K}^T \tag{7}$$

where $\boldsymbol{K}$ is the Kalman gain that is calculated based on $\hat{\boldsymbol{P}}_k$, $\boldsymbol{R}$, the measurement covariance, and the $\boldsymbol{H}$, the Jacobian matrix of the observation model (shown in Eq. 2) over the vehicle states.

B. EKF Setup

In the first step, we calibrated the magnetometer in the AHRS at the testing site to correct for the hard iron bias. In the tests, we used the raw IMU data and the Madgwick Filter [29] to perform the pose estimation.

Nortek DVL bottom-track velocities [30] and depth measurements from its pressure sensor are used in our odometry estimation. The bottom-track velocities are sound-speed corrected as the default sound-speed is configured at 1500m/s and the actual sound speed is 1417m/s at our testing site. The pressure measurements are "zeroed" at the water surface to remove the pressure bias.

The diagonal elements in the process noise covariance, Q, is presented in Tab. I. Since the DVL, AHRS and the Base (located at the rear-back corner), are located at different locations, we used the TF ROS package to transform data between the frames. The values for the transformation is presented in Tab. II.

TABLE I
PROCESS NOISE COVARIANCE MATRIX DIAGONAL VALUES.

$Q_{0,0}$	$1e^{-8}$	$Q_{1,1}$	$1e^{-8}$	$Q_{2,2}$	0.9
$Q_{3,3}$	0.3	$Q_{4,4}$	0.3	$Q_{5,5}$	0.9
$Q_{6,6}$	0.5	$Q_{7,7}$	0.5	$Q_{8,8}$	0.3
$Q_{9,9}$	0.3	$Q_{10,10}$	0.3	$Q_{11,11}$	0.3
$Q_{12,12}$	0.3	$Q_{13,13}$	0.3	$Q_{14,14}$	0.3

TABLE II
TRANSFORMS BETWEEN BASE AND DVL, DVL AND AHRS.

	$x(m)$	$y(m)$	$z(m)$	$\phi(rad)$	$\theta(rad)$	$\psi(rad)$
Base−DVL	-0.139	0.172	0.391	0.0	0.0	0.0
DVL−AHRS	0.434	-0.088	-0.301	3.132	0.003	3.13

V. PRELIMINARY FIELD RESULTS

In March 2021, field experiments were carried out in the Keweenaw Waterway, Michigan, where the ice thickness is about 10 to 12 inches. As shown in Fig. 2, multiple ice-holes were drilled in a straight line on the ice surface. The largest ice-hole was used for ROV deployment, while the others were mainly designed to place artificial targets with AR tags [31] that could provide ground truth information for post-processing camera images. Field tests were conducted at different locations and various weather conditions that helped us to understand how the illumination affects the under-ice images.

During the deployment, the ROV was remotely controlled using sonar images as shown in Fig. 2, and upward-looking cameras to navigate the ROV along the artifical targets we placed at 10 to 20 meter intervals. In order to capture clear ice features safely, the ROV was kept to move within 2-3 meters off the ice. The ROV was piloted to move back-and-forth in a straight-line multiple times.

We applied the EKF-based odometry estimator mentioned in Section IV, and Fig. 3 presents the resulting vehicle trajectory. We noticed moderate drift while the ROV is moving at a slow speed which could be observed at the end of the transects. In order to quantify the errors in the odometry, we have tried existing visual odometry algorithms, e.g., ORB-SLAM [32], but the result was not satisfying and the algorithm failed to track and match features in such a low-contrast images. As discussed in Section VI, other feature detection and image processing algorithms needs to be developed.

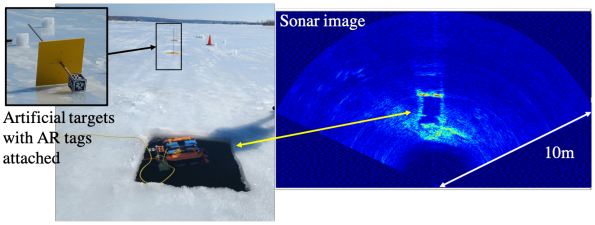

Fig. 2. The ROV deployed through an ice hole. Artificial targets are set along ROV's move track. (Image credit to Brice Loose)

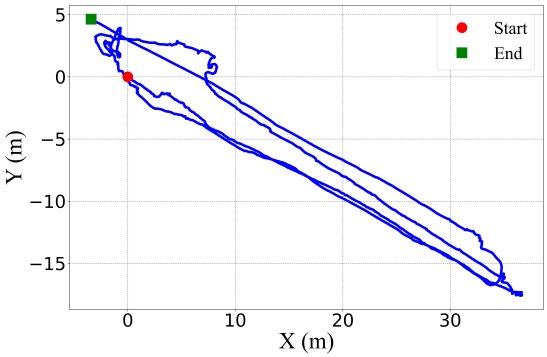

(a)

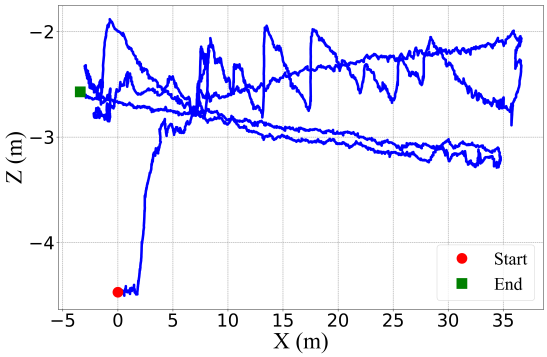

(b)

Fig. 3. EKF Odometry based om AHRS, DVL and the pressure sensor. The ROV was deployed and recovered from the same ice hole. a) Top view, (b) X-Z plane.The X-Y plane error distance in the odometry between the start and the end points is 5.75 m.

In here, we could validate our odometry using the images with observation of the same ice-hole or ice-block, but collected at different times. As shown in Fig. 4, we presented two pairs of images that were take at different time but containing the same feature. Therefore, the images in each pair should be taken at a similar location.

The EKF odometry at these selected positions is displayed in Fig. 5. In Tab. III, we show the X-Y distance errors between

the odometry at each paired locations. The averaged error is about 2 meters and 4.5 meters for two transects. We also calculated the drift rate which is the average distance error divided by the average distance travelled between each pair of image for every transect. The overall travelled distance in the mission is about 200 meters, all the travel distance are calculated based on the EKF odometry.

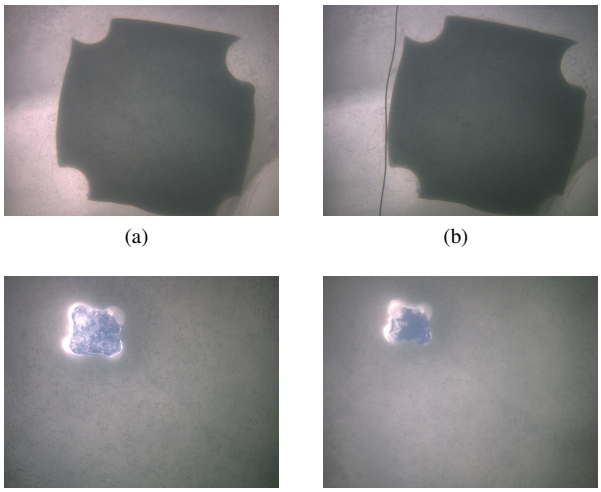

(a) (b) (c) (d)

Fig. 4. Image pairs for slected positions. (a) and (b) are the first pair of images with ice-block observed at different times; (c) and (d) are the fourth image pairs with ice-hole observed at different times.

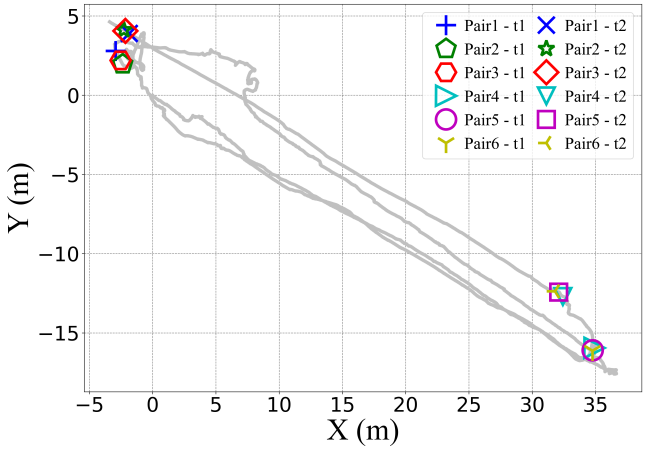

Fig. 5. The top view of the EKF odometry with the locations of the selected image pairs shown in different marker styles.

Besides the current profile and the bottom-track, the DVL also provides a rough estimate of the distance between the ROV and the bottom of the ice. Using such distance measurements and the EKF estimated depth, we estimated the ice thickness. The result is shown in Fig. 6. The DVL ranges are corrected using the sound speed as mentioned in Section IV, and the DVL's mounting offsets are also measured and corrected to provide an accurate ice thickness measurements. As seen in Fig. 6, the ice thikcness averaged from 4 beam measurements contains noise in some locations, where the ice-holes are located. The noise is mainly caused by the multi-path at the water openings. This condition can be observed in Fig. 6 at time 580 seconds when the ROV is moving beneath the deployment ice-hole. Least squares line fitting is applied to estimated ice thickness from noise ice thickness. As shown in Fig. 6, it indicated the flat ice keel has a roughly 0.3m thickness, which agrees with our manual observation while driling ice holes.

TABLE III
EKF ODOMETRY ERROR IN X-Y PLANE, UNIT: (M)

	Pair 1	Pair 2	Pair 3	Pair 4	Pair 5	Pair 6
Err.	1.542	2.156	1.895	4.096	4.544	4.782
Avg. Err.	1.864			4.474		
Dis.	101.948	101.318	101.646	117.308	117.492	117.755
Avg. Dis.	101.637			117.518		
Drift Rate	1.83%			3.49%		

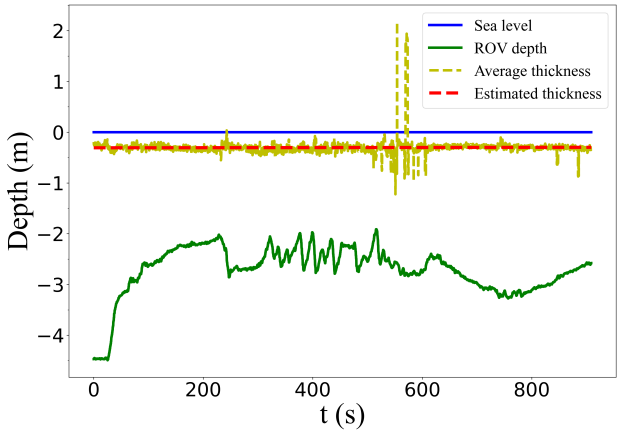

Fig. 6. ROV depths over time (Green), and ice thickness measurements (yellow and red)

One important purpose of this mission is to gather under-ice visual and acoustic images for developing feature tracking and target detection algorithms. As shown in Fig. 2, imaging sonar is capable of detecting ice openings. The ice-hole edge is highlighted as rectangle, and the other patch of bright area is due to an ice block that was pushed below the ice. The rough ice-hole edge and relative smooth ice will have diffusion and specular reflection respectively, this reflection property will also help to make acoustic fiducial marker [33].

Stereo camera images captured the ice-hole, around 6 inches, are shown in Fig. 4. During this mission, the light field is sufficient such that onboard LED were no longer needed. Also, we removed the artificial target since those AR tags were dark due to the natural light coming from above. We expect vision-aided solution [34] will increase the navigation accuracy compare to inertial sensor solution. Ice features, such as the air bubbles, are visible in the images when the ROV maintained within 2 meters to the ice. However, those features are ubiquitous and similar in the image, descriptor-

based tracking, e.g., the ORB-SLAM, was not capable of tracking and matching these features from our test.

VI. Conclusion and future works

In this paper, we demonstrated the upgraded ROV with multi-modality sensors for under-ice environment research. The collected filed data including stereo images and sonar images were displayed. An EKF navigation is implemented with result shown in the paper. By comparing to the camera images collected at the same location but different times, we estimated the odometry errors. The average errors are about 2 meters and 4.5 meters at different locations on the transects and drift rate are around 1.83% and 3.49%.

Currently, we are integrating other visual odometry methods, e.g., the Kanade–Lucas–Tomasi (KLT) [35]. We will also explore new image processing algorithms to highlight the air bubbles and other textures to reduce drift by introducing the loop-closure. We will also examine the usage of sonar images to provide additional feature constraints to improve the localization precision. In March 2022, we plan to perform additional field experiments to test our developed algorithms.

References

[1] G. A. MacGilchrist, A. C. Naveira Garabato, T. Tsubouchi, S. Bacon, S. Torres-Valdés, and K. Azetsu-Scott, "The Arctic Ocean carbon sink," Deep Sea Research Part I: Oceanographic Research Papers, vol. 86, pp. 39–55, Apr. 2014.

[2] D. Lannuzel et al., "The future of Arctic sea-ice biogeochemistry and ice-associated ecosystems," Nat. Clim. Chang., vol. 10, no. 11, pp. 983–992, Nov. 2020, doi: 10.1038/s41558-020-00940-4.

[3] A. Boetius et al., "Export of Algal Biomass from the Melting Arctic Sea Ice," Science, vol. 339, no. 6126, pp. 1430–1432, Mar. 2013, doi: 10.1126/science.1231346.

[4] M. Vancoppenolle et al., "Role of sea ice in global biogeochemical cycles: emerging views and challenges," Quaternary Science Reviews, vol. 79, pp. 207–230, Nov. 2013, doi: 10.1016/j.quascirev.2013.04.011.

[5] P. Assmy et al., "Leads in Arctic pack ice enable early phytoplankton blooms below snow-covered sea ice," Sci Rep, vol. 7, no. 1, p. 40850, Feb. 2017, doi: 10.1038/srep40850.

[6] R. Krishfield, J. Toole, A. Proshutinsky, and M.-L. Timmermans, "Automated Ice-Tethered Profilers for Seawater Observations under Pack Ice in All Seasons," Journal of Atmospheric and Oceanic Technology, vol. 25, no. 11, pp. 2091–2105, Nov. 2008, doi: 10.1175/2008JTECHO587.1.

[7] M. Nakawo, "Measurements on Air Porosity of Sea Ice," Ann. Glaciol., vol. 4, pp. 204–208, 1983.

[8] M. Hoppmann, M. E. Richter, I. Smith, S. Jendersie, P. J. Langhorne, D. N. Thomas and G. S. Dieckmann, "Platelet ice, the Southern Ocean's hidden ice: a review," Ann. Glaciol., pp. 1–28, Oct. 2020.

[9] B. Loose, A. Garabato, P. Schlosser, W. Jenkins, D. Vaughan, and K. Heywood, "Evidence of an active volcanic heat source beneath the Pine Island Glacier," NATURE COMMUNICATIONS, vol. 9, no. 2431, 2018.

[10] R. Krishfield et al., Design and operation of automated ice-tethered profilers for real-time seawater observations in the polar oceans. Woods Hole, MA: Woods Hole Oceanographic Institution, 2006.

[11] L. A. Miller et al., "Methods for biogeochemical studies of sea ice: The state of the art, caveats, and recommendations," Elementa: Science of the Anthropocene, vol. 3, p. 000038, Jan. 2015, doi: 10.12952/journal.elementa.000038.

[12] P. Norgren, R. Lubbad, and R. Skjetne, "Unmanned underwater vehicles in Arctic operations," in 22nd IAHR International Symposium on Ice, Singapore, 2014, p. 14.

[13] B. Bulter (2018), "Into the Labyrinth, the Making of a Modern-Day Theseus", Bigfoot Press, Canada.

[14] P. Wadhams, J. P. Wilkinson, and A. Kaletzky, "Sidescan Sonar Imagery of the Winter Marginal Ice Zone Obtained from an AUV," JOURNAL OF ATMOSPHERIC AND OCEANIC TECHNOLOGY, vol. 21, p. 9, 2004.

[15] S. D. McPhail et al., "Exploring beneath the PIG Ice Shelf with the Autosub3 AUV," in OCEANS 2009-EUROPE, Bremen, Germany, May 2009, pp. 1–8. doi: 10.1109/OCEANSE.2009.5278170.

[16] A. B. Phillips, M. Kingsland, N. Linton, W. Baker, L. Bowring, S. Soper, et. al., "Autosub 2000 Under Ice: Design of a New Work Class AUV for Under Ice Exploration," in 2020 IEEE/OES Autonomous Underwater Vehicles Symposium (AUV)(50043), St Johns, NL, Canada, Sep. 2020, pp. 1–8.

[17] Kangsoo Kim et al., "Towards AUV-based iceberg profiling and gouging survey in arctic sea: The first Japanese under-ice AUV deployment in Okhotsk Sea," in 2013 IEEE International Underwater Technology Symposium (UT), Tokyo, Mar. 2013, pp. 1–5. doi: 10.1109/UT.2013.6519870.

[18] G. Williams, T. Maksym, J. Wilkinson, C. Kunz, C. Murphy, P. Kimball and H. Singh, "Thick and deformed Antarctic sea ice mapped with autonomous underwater vehicles," Nature Geosci, vol. 8, no. 1, pp. 61–67, Jan. 2015.

[19] H. Singh, T. Maksym, J. Wilkinson, and G. Williams, "Inexpensive, small AUVs for studying ice-covered polar environments," Sci. Robot., vol. 2, no. 7, Art. no. 7, Jun. 2017, doi: 10.1126/scirobotics.aan4809.

[20] A. Wahlin, B. Queste, A. Graham, K. Hogan, L. Boehme, K. Heywood, R. Larter, E. Pettit, J. Weliner, "Warm water flow and mixing beneath Thwaite Glacier ice shelf, West Antarctica", EGU General Assembly Conference Abstracts.

[21] A. L. Forrest, B. Laval, M. J. Doble, R. Yeo, and E. Magnusson, "AUV measurements of under-ice thermal structure," in OCEANS 2008, Quebec City, QC, Canada, 2008, pp. 1–10. doi: 10.1109/OCEANS.2008.5152046.

[22] A. L. Forrest et al., "Digital terrain mapping of Petermann Ice Island fragments in the Canadian High Arctic," in 21st IAHR International Symposium on Ice, 2012, p. 13.

[23] M. J. Doble, A. L. Forrest, P. Wadhams, and B. E. Laval, "Through-ice AUV deployment: Operational and technical experience from two seasons of Arctic fieldwork," Cold Regions Science and Technology, vol. 56, no. 2–3, pp. 90–97, May 2009, doi: 10.1016/j.coldregions.2008.11.006.

[24] A. Kukulya et al., "Under-ice Operations with a REMUS-100 AUV in the Arctic," in IEEE/OES AUV2010, 2010, p. 8.

[25] S. E. Webster, L. E. Freitag, C. M. Lee, and J. I. Gobat, "Towards real-time under-ice acoustic navigation at mesoscale ranges," in 2015 IEEE International Conference on Robotics and Automation (ICRA), Seattle, WA, USA, May 2015, pp. 537–544

[26] A. Spears, M. West, M. Meister, C. Walker, J. Buffo, T. Colins, A. Howard and B. Schmidt, "Under Ice in Antarctica: The Icefin Unmanned Underwater Vehicle Development and Deployment," IEEE Robot. Automat. Mag., vol. 23, no. 4, Art. no. 4, 2016.

[27] R. E. Kalman, "A New Approach to Linear Filtering and Prediction Problems," J. Basic Eng., vol. 82, no. 1, pp. 35–45, 1960.

[28] T. Moore, D. Stouch, "A Generalized Extended Kalman Filter Implementation for the Robot Operating System," Intelligent Autonomous Systems 13, Advances in Intelligent Systems and Computing, vol. 302, pp. 335–348, 2016.

[29] S. Madgwick, "An efficient orientation filter for inertial and inertial/magnetic sensor arrays," Report x-io and University of Bristol (UK), 2010.

[30] L. DL. Barker, L. L. Whitcomb, "A Performance Analysis of Ice-Relative Upward-Looking Doppler Navigation of Underwater Vehicles Beneath Moving Sea Ice," Journal of Marine Science and Engineering, 2021.

[31] J. Wang, E. Olson, "AprilTag 2: Efficient and robust fiducial detection," 2016 IEEE/RSJ International Conference on Intelligent Robots and Systems (IROS), pp. 4193-4198, 2016.

[32] R. Mur-Artal and J. D. Tardós, "ORB-SLAM2: An Open-Source SLAM System for Monocular, Stereo, and RGB-D Cameras," in IEEE Transactions on Robotics, vol. 33, no. 5, pp. 1255-1262, Oct. 2017.

[33] Y. Wang, Y. Ji, D. Liu, Y. Tamura, H. Tsuchiya, A. Yamashita, H, Asama, "ACMarker: Acoustic Camera-Based Fiducial Marker System in Underwater Environment," in IEEE Robotics and Automation Letters, vol. 5, no. 4, pp. 5018-5025, Oct. 2020

[34] P. Geneva, K. Eckenhoff, W. Lee, Y. Yang and G. Huang, "OpenVINS: A Research Platform for Visual-Inertial Estimation," 2020 IEEE International Conference on Robotics and Automation (ICRA), pp. 4666-4672, 2020.

[35] B.D. Lucas and T. Kanade. "An Iterative Image Registration Technique with an Application to Stereo Vision," International Joint Conference on Artificial Intelligence, pages 674–679, 1981.